The role of β-Zr in a Zr-2.5Nb alloy during aqueous corrosion: A multi-technique study

Junliang Liu[1, *], Guanze He[1, §], Anne Callow[1], Kexue Li[2], Katie L. Moore[2], Heidi Nordin[3], Michael Moody[1], Sergio Lozano-Perez[1], Chris R. M. Grovenor[1]

[1]Department of Materials, University of Oxford, Oxford, OX1 3PH, UK.

[2]Department of Materials and Photon Science Institute, University of Manchester, Manchester, M13 9PL, UK.

[3]Canadian Nuclear Laboratories, Chalk River, Ontario, K0J 1J0, Canada.

* junliang.liu@materials.ox.ac.uk, § guanze.he@materials.ox.ac.uk

Abstract

The Zr–2.5Nb alloy is used as pressure tubes in Canadian Deuterium Uranium (CANDU) nuclear reactors, and the typical starting microstructure consists of α-Zr grains elongated in both transverse and longitudinal directions and thin layers of partially decomposed β-Zr lying between the α-Zr grains. In this study, we have used state-of-the-art microscopy techniques to characterise the long-term thermally decomposed β phase in this alloy, and the oxide scale formed on them in a reactor coolant loop with the aim of understanding the mechanisms underpinning the thermal decomposition behaviour at service temperatures and exploring the role of the decomposed β-Zr phase in controlling the microstructure and microchemistry of the zirconium oxide, and hence its influence on the general corrosion resistance of the alloy. We observe that these β-Zr layers are heavily decomposed even after the short stress stage at 400°C at the end of the manufacturing cycle, with a closely packed array of β-Nb precipitates forming in an α-Zr matrix. We have shown that the oxidation of these bands is significantly slower than the surrounding α-Zr matrix and that zirconium oxide grains are re-nucleated under each band. We conclude that it is the combination of the Nb-rich remnants of the original β-Zr layers arising from the hot extrusion and drawing stages and this new dense oxide that offers a significant barrier to the oxidation front (and also to the penetration of hydrogenic species), so the characteristic layered microstructure arising from the original manufacturing process is very important in determining the overall oxidation behaviour.

1. Introduction

Zirconium alloys have been selected as components in nuclear reactors for decades because of their low neutron capture cross-section, and reasonable mechanical properties and corrosion resistance [1]. Despite a successful service history, an improvement in the in-reactor corrosion resistance is still desired by the nuclear industry because of the development of the high burn-up fuels [2], and the need for life extension on reactor internals. Zr-Nb alloys can show much better resistance to corrosion under reactor conditions than the Sn-containing Zircaloy family [3], and hence have been extensively studied in recent years.

Depending on their thermo-mechanical history, a range of different microstructures are found in the various classes of nuclear Zr-Nb alloys. Almost all of them have an α-Zr matrix, but if they are quenched from the high temperature β region during the manufacturing process, they will contain the high temperature β-Zr phase (or its decomposition products) in the final microstructure. Zr-Nb alloys can therefore be divided into two general categories: those recrystallised below the monotectoid temperature which only contain the equilibrium β-Nb phase in the form of small second phase precipitates (SPPs) such as E110, ZIRLO, M5 [4–7]; and the β-quenched and annealed alloys that contain some residual β-Zr phase such as the Zr-2.5Nb and Zr-Excel alloys used in the CANDU reactors [8–10]. The morphology of the β-Zr phase also depends on the manufacturing route. In Zr-Excel alloy, the β-Zr is commonly nucleated at grain boundary triple points [10], while in the CANDU Zr-2.5Nb pressure tube alloys this phase is found in sheets parallel to the axial and hoop directions as a result of deformation after the beta-quenching [9]. The role that this unique morphology of the decomposition products of the β-Zr can play in determining the corrosion resistance of the alloy is the focus of this paper.

While the presence of β-Nb SPPs is generally considered beneficial to the corrosion resistance in recrystallised Zr-Nb alloys [5,6,11], the role of residual β-Zr in controlling the corrosion performance of annealed Zr-Nb alloys is not so straightforward. It has been stated that the oxidation of β-Zr phase in Zr-2.5Nb alloys can lead to a very complex local microstructure including a variety of oxide phases [12], and accelerate the overall corrosion rates by favouring

the formation of equiaxed oxide grains [6]. Alloys with different state of β-Zr decomposition are reported to show different corrosion and hydrogen pickup rates [13,14]. At in-service temperatures, metastable β-Zr is expected to continue to decompose [15], and the longer the β phase spends in the metal matrix under reactor conditions, and hence the more decomposed it becomes, the more significantly it can affect the overall corrosion performance of Zr alloys [14]. There is clearly a need for a better understanding of the thermal decomposition behaviour of metastable β-Zr at in-service temperatures and its role in determining the mechanisms of corrosion in Zr-Nb alloys of this type, taking into account the effects of both microstructure and phase chemistry.

The development of new advanced characterisation techniques in recent years has allowed researchers to investigate the corrosion behaviour of Zr alloys in unprecedented detail. Microstructural features that were hard to study previously, such as the precise identification of suboxides at the metal/oxide interface, oxide saturated regions in the underlying metal and phase distributions in the zirconium oxide, have been studied in detail in Zr alloy systems. However, few of these techniques have been applied to the study of metastable β-Zr in annealed Zr-Nb alloys. Here we have used state-of-the-art microscopy techniques to characterise the long-term thermally decomposed β phase in a Zr-2.5Nb alloy, and the oxide scale formed on this alloy under reactor coolant loop conditions but without neutron irradiation, with the aim of exploring the role of the β-Zr in controlling the microstructure and microchemistry of the zirconium oxide, and its influence on the general corrosion resistance of the alloy.

2. Materials and Experiments

2.1. Materials

The Zr-2.5Nb alloy used in this study was provided by Canadian Nuclear Laboratories (CNL). This pressure tube material was fabricated from ingots made by ATI Wah Chang using the Kroll process with two stages of vacuum arc melting (double melt ingot) [8]. Forging is used to convert cast ingots into logs that are 280 cm long by 21 cm in diameter, and the logs machined to produce billets which were heated to 1015°C and then water quenched (beta-quenched). The

solid billets were then trepanned and extruded at 815°C, straightened and cold drawn by 27% to produce tubes that are 6 m long with an outside diameter of 11.2 cm. These extruded tubes are finally stress relieved at 400°C for 24 hours. As a result of the extrusion process, this Zr-2.5Nb alloy shows a strong crystallographic texture with the α-Zr [0002] pole aligned with the transverse direction as shown in Figure 1 in section 3.1 and reported by Cheadle [8] and Judge et. al. [16]. This characteristic texture is rather different to that found in other Zr cladding alloys used in PWRs that have a different thermomechanical history and a texture with the [0002] pole close to the radial direction [17].

Corrosion coupons were machined from these pressure tubes and degreased by ultrasonically cleaning in acetone and then rinsing in deionized water. A pre filming process, which involved heating the coupons at 400°C for 24 hours in 0.7 MPa light water steam, was used to produce a thin layer of adherent surface oxide. Out-of-flux coupons (labelled as Halden out-of-flux in Table 1) were corroded in the Halden test reactor under reactor coolant loop conditions (D_2O, $pH_{25°C} \approx 10.5$, LiOH) but without neutron irradiation for up to 2858 days at 325°C and 10 MPa. Autoclaved coupons (labelled as Autoclave corrosion in Table 1) were exposed in a static autoclave filled with D_2O ($pH_{25°C} \approx 10.5$, LiOH) at 300°C and 10 MPa for up to 2000 days. Table 1 gives the details of the samples selected for microstructural characterisation and analysis.

Table 1 Selected samples at different stages of oxidation for microstructural analysis

Sample ID	Status	Corrosion time (days)	Oxide thickness (μm)	Analysis techniques
2.5Nb-1	Starting alloy	-	-	STEM, EDX, APT
2.5Nb-2	Halden out-of-flux	185	2.4	(S)TEM, TKD
2.5Nb-3	Halden out-of-flux	2858	16.0	(S)TEM, APT
2.5Nb-4	Autoclave corrosion	700	3.7	SIMS

2.2. Specimen preparation

The Halden out-of-flux corroded coupons have a rather modest measured activity, $\sim 1.15 \times 10^2$ Bq for sample 2.5Nb-2, and so a shielded Thermal Fisher Helios Nanolab 600i FIB/SEM system at the Materials Research Facility (MRF, https://mrf.ukaea.uk/) at the Culham Centre

for Fusion Energy (CCFE) was used to extract small samples for microstructural analysis. TEM foils are prepared using the in-situ FIB lift-out method with an initial focused ion beam milling current of 9 nA, gradually decreasing to 230 pA at 30 kV, and further thinned to a uniform thickness of ~50 nm using a low energy beam at 2 kV and 300 pA. Detailed step-by-step instructions describing these specimen preparation protocols in the FIB are given in [18]. APT samples were prepared using a standard cantilever lift-out technique [19]. Sections of cantilever 2 µm thick were mounted onto pre-fabricated Si-microposts using W deposition. Samples were then thinned to around 400 nm diameter using an annular milling pattern with 30 kV probe with incremental reduction in current from 700 pA to 80 pA. Sharpening into needle shaped APT tips was carried out using a 2 kV: 300 pA probe at low magnification so that the final tip apex was below 100 nm in diameter. Samples were prepared for TEM and APT analysis from the inactive materials (2.5Nb-1) using Zeiss Crossbeam 540 FIB/SEM and Zeiss NVision 40 systems following similar procedures.

Autoclaved sample 2.5Nb-4 was selected for high resolution SIMS analysis to study the distribution of Li in the oxide layer. Samples for NanoSIMS analysis of size 7.2 × 7.2 mm^2 were cut from the corroded materials using a slow speed diamond saw, and coated with 5 nm of platinum to minimise charging from the insulating oxide layer.

2.3. Microstructure characterization methods

2.3.1. Transmission electron microscopy (TEM)

A JEOL 2100 microscope operated at 200 kV was used to carry out nano-beam diffraction (NBD) analysis of decomposed β-Zr phases and Fresnel contrast analysis of nano-porosity in the oxide layers. Fresnel contrast in the conventional TEM in bright-field mode originates from the difference in the inner potential of the matrix and the cavity, and depends on the effective thickness variations in the direction of the incident electron beam [20,21]. When the image is over-focused, black fringes appear around a cavity, or white fringes when the image is under-focused. Energy-dispersive X-ray (EDX) spectrometry analysis was performed using a JEOL 3000F transmission electron microscope operating at 300 kV. High-angle annular dark-field

(HAADF) imaging has its contrast sensitive to local variations of average atomic mass (intensity of each pixel $\propto Z^2$, where Z is the average atomic number), so-called Z-contrast [22], and is used to show these Nb-enriched β-Zr regions. HAADF images were acquired using a JEOL JEM-ARM200F scanning transmission electron microscope (STEM) operated at 200 kV. Low-loss electron energy loss spectroscopy (EELS) and multiple linear least squares (MLLS) fitting [23] can be used to map the distribution of the different phases, e.g. ZrO_2, ZrO suboxide, oxygen-saturated zirconium and zirconium metal, from a large sample area at a pixel size of few nanometres. The EELS low-loss spectra used for this MLLS fitting were acquired using a JEOL ARM200F microscope (200kV, CFEG source, Cs probe corrected) equipped with a Gatan Imaging Filter (GIF), with a convergence angle of 31 mrad, a collection angle of 41 mrad, an energy dispersion of 0.25 eV/channel and a pixel size of 5 nm. MLLS fitting was carried out using the script in Digital Micrograph (DM) developed by Gatan Inc.

2.3.2. Atom Probe Tomography (APT)

Atom probe tomography (APT) permits the chemical analysis of very small volumes of matrials with near atomic resolution [24], and has been widely used to explore the chemical composition of nanoscale precipitates [25,26]. All APT samples in this study were analysed using a Cameca LEAP 5000 XR atom probe in laser pulsed mode using a tip temperature of 55-60 K, 55-65 pJ laser energy and a laser pulsing frequency of 125 kHz. Compositions were found using mass-spectrum peak decomposition to address the Nb^{2+}/ZrH^{2+} overlap at 46.5 Da, and Fe was ranged in the Fe^{2+} charge state only. Small precipitates were isolated using a maximum separation algorithm using the parameters shown in Table 2. Eleven APT datasets were analysed to measure the chemical composition of the starting alloy (Sample 2.5Nb-1). Seven of the datasets containing only the α-Zr matrix were analysed to determine the matrix composition with a total of 14 million ions (a total volume of 6.28×10^{-16} cm^3). The other four separate APT datasets contained both α-Zr matrix and decomposed β-Zr regions. The Nb-enriched β phase was extracted using a 55 at% Nb iso-concentration surface using Cameca IVAS APT data analysis software, and the Nb-depleted regions extracted using a 1.5 at% Nb iso-concentration surface.

In the Nb-enriched β-Zr phase a volume of 2.74×10^{-17} cm^3 was analysed in total, and a volume of 9.74×10^{-17} cm^3 from the Nb-depleted phase. Similar analysis was used to calculate the average composition of a long-term corroded sample 2.5Nb-3, analysing a volume of 1.34×10^{-17} cm^3 of the Nb-enriched phase, and a volume of 4.03×10^{-17} cm^3 of the surrounding Nb-depleted matrix. Only one of these three datasets contained the decomposed β-Zr phase. All APT quantification data errors are quoted as one standard deviation.

Table 2 Precipitate segmentation parameters

Ions	D_{max} (nm)	N_{min}	Order	$L/d_{erosion}$ (nm)
Fe^{2+}, Cr^{1+}, Cr^{2+}, Mn^{2+}, V^{2+}	0.9	15	1	0.45

2.3.3. Transmission Kikuchi diffraction (TKD)

TKD characterization was carried out on a Zeiss Merlin FEG-SEM system equipped with a Bruker OPTIMUS™ TKD head and a e-flash high resolution Electron Backscatter Diffraction (EBSD) detector [27]. The accelerating voltage was set to 30 kV and a probe current of 1.5 nA used to acquire Kikuchi patterns with resolution 320 × 200 using a pixel time of 9.3 ms. A step size of 5 nm was used to enable the characterization of nano-crystalline grains. The TKD maps were further cleaned using the Oxford Instruments HKL Channel 5 software package to remove isolated pixels that were incorrectly indexed or not solved. The crystallographic information used in identifying the phase distribution in the samples has been given in [28].

2.3.4. High-resolution Secondary Ion Mass Spectrometry (NanoSIMS)

NanoSIMS measurements were performed with a Cameca NanoSIMS 50L instrument equipped with a Hyperion RF-plasma ion source (Oregon Physics) to generate an O^- primary ion beam to maximise the secondary ion yield from positive ions. Primary ions were accelerated to +16 keV. The D1 capture was set to D1-2 with the size of 300 µm in diameter, the primary current was 14.5 pA with a beam diameter of approximately 150 nm. The mass spectrometer was aligned to detect the $^{7}Li^{+}$ and $^{93}Nb^{+}$ signals. The Entrance slits, aperture slits and energy slits were set to ES-3, AS-2 and open, respectively. The analysis protocols used in this study were

similar to those described in [29]. During SIMS measurements, the primary ion beam was scanned over 256 × 256 pixels with 1000 µs/pixel dwell time over a raster area of 5×5 μm^2, and the sputtered secondary ions were collected by the mass spectrometer. This scanning process was repeated 1000 times in the analysis region to remove a total thickness of 2-3 µm, resulting in a serial of images with the measured values for the counts from each secondary ion in each pixel/voxel. ImageJ with the OpenMIMS plugin [30] was used to align these images, create in-depth profiles and cross-sectional views.

3. Results and discussion

3.1. Initial microstructure of the as-received alloy

Figure 1 shows STEM, EDX and TKD maps from the as-received Zr-2.5Nb metal matrix (Sample 2.5Nb-1). Cooling from the extrusion process at 815°C results in an elongated two phase α-Zr and β-Zr microstructure when viewed along the transverse direction (TD) of the tube, Figure 1 (a). Most of the β phase transforms to α during the air-cooling stage, and since niobium has a low solubility in α (0.6 wt %) [31], the remaining β phase becomes further enriched in Nb. HAADF imaging that is sensitive to average atomic mass shows up these Nb-enriched β-Zr regions by brighter contrast, Figure 1 (a and b). The β phase is present as thin layers between the elongated α-Zr grains and has an average thickness of 50-200 nm, Figure 1 (a). Micro-texture analysis on such small grains using normal electron backscatter diffraction (EBSD) or off-axis TKD is challenging due to its limited spatial resolution [16], but the on-axis TKD used here can clearly separate the two phases with different crystal structures, Figure 1 (d), and analyse texture at the nanoscale in both phases (see [32] for more details about the on-axis TKD). Figure 1 (e) shows the inverse pole figure (IPF) maps along the TD. The majority of α-Zr grains have their basal plane normal close to the TD of the tube, which is very different to the crystallographic texture of fuel cladding alloys like Zircaloy-2 and Zircaloy-4 where the basal plane normal are usually close to the radial direction (RD) [17]. The crystallographic texture of this Zr-2.5Nb pressure tube is shown schematically in Figure 1 (f). The relationship between α-Zr and β-Zr is close to the Burgers orientation relationship $(0002)_{\alpha\text{-}Zr} \| (110)_{\beta\text{-}Zr}$ and

$(2\bar{1}\bar{1}0)_{\alpha\text{-}Zr} \| (1\bar{1}1)_{\beta\text{-}Zr}$. All of these microstructural features, the crystallographic texture of the α grains, the shape and size of the α grains, the distribution of the metastable β phase and segregation of alloying and impurity elements can affect the in-service behaviour of this Zr-2.5Nb alloy.

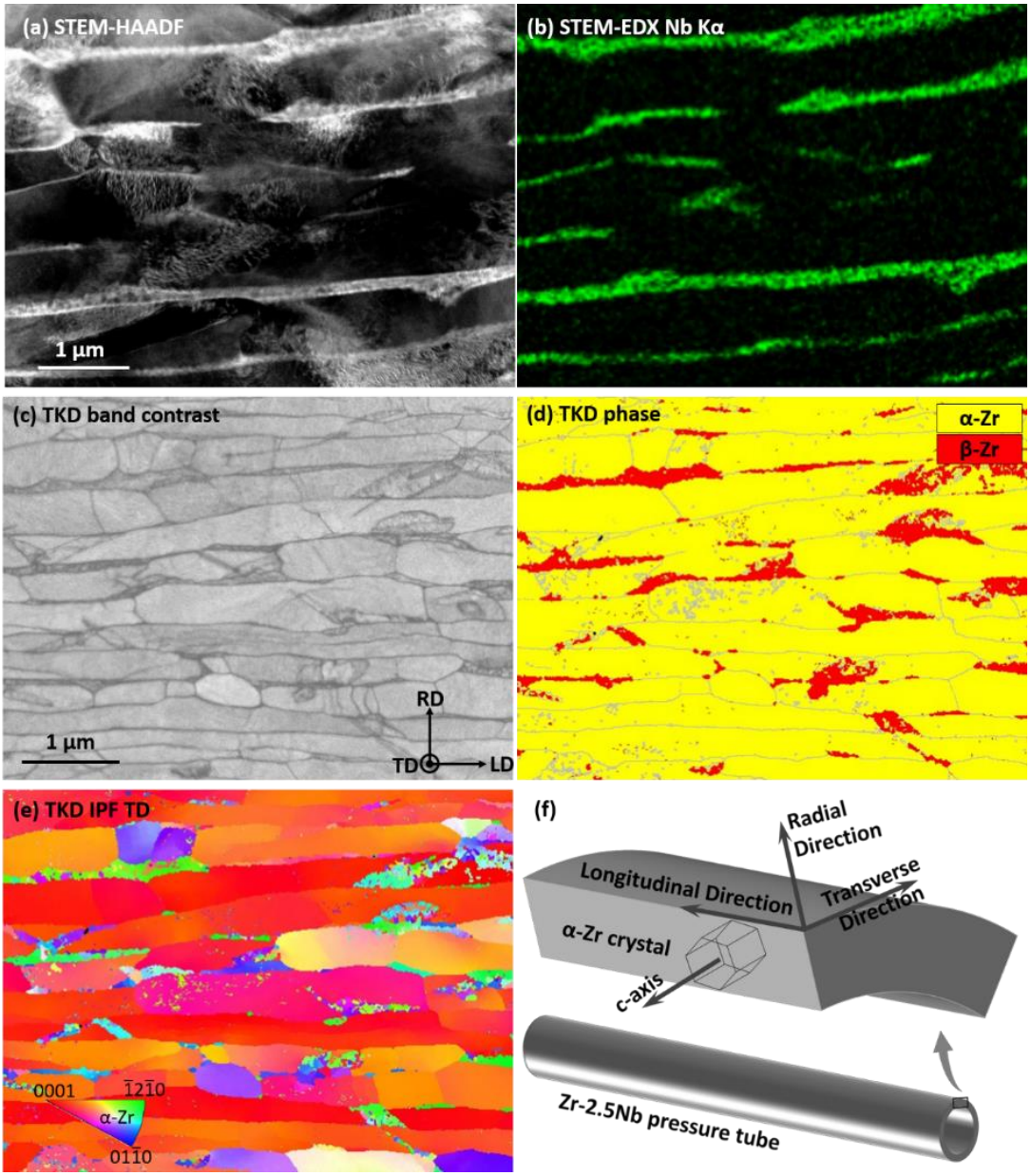

Figure 1 (a, b) Typical STEM-HAADF image and EDX map, (c) TKD band contrast map, (d) phase map, (e) inverse pole figure along the transverse direction showing the microstructure and Nb distribution in the sample 2.5Nb-1. (f) A schematic showing the matrix crystal orientation in the Zr-2.5Nb pressure tube.

3.2. Thermal decomposition of the β-Zr phase

Based on the Zr-Nb equilibrium phase diagram [31] the manufacturing process leads to a two-phase structure consisting of stable α-Zr grains and a grain boundary network of metastable β-

Zr. This β-phase will transform into other phases with time below 600°C, and a general decomposition process [33] has been described as,

$$\beta\text{-Zr} \rightarrow \omega\text{-Zr} + \beta\text{-Zr (Nb enriched)} \rightarrow \beta\text{-Nb} + \alpha\text{-Zr}$$

The microstructure of second phases in Zr alloys has a profound influence on their corrosion behaviour [6,13,33], and a considerable body of research has studied the microstructural changes in Zr-2.5Nb alloys during heat-treatment, thermal decomposition or irradiation, especially in the temperature range from 400°C to 600°C for relatively short times (up to hundreds of hours) [13–15,34,35]. The decomposition behaviour of β-Zr at in-service temperatures over much longer time (more closely corresponding to the real in-service situation) has been less reported.

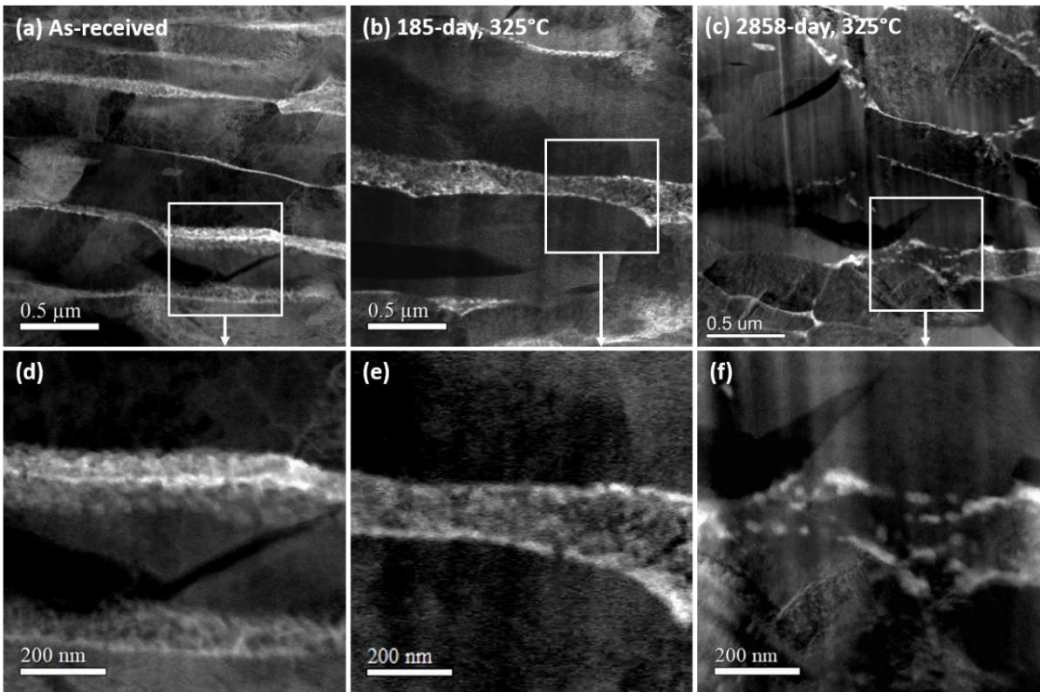

Figure 2 STEM-HAADF images showing morphologies of the Nb-enriched phases in the metal matrix of the Zr-2.5Nb alloy after different times in high temperature water, (a) 2.5Nb-1, (b) 2.5Nb-2 and (c) 2.5Nb-3. (d, e and f) are enlarged images showing the Nb-enriched phases from the region highlighted in (a, b and c). The Nb-rich phase shows brighter contrast in the HAADF images because they have a higher average atomic mass compared to the surrounding metal matrix.

It has been previously reported [35–37] that the final stress-relief treatment (400°C for 24 h) and pre-filming process (also 400°C for 24 h) results in partial decomposition of the original layers of β-Zr into a complex network of α-Zr, Nb-enriched β-Zr, equilibrium highly Nb-rich

β-Nb and intermediate ω-Zr. Typical HAADF images of the microstructure of the decomposed phases in our material corresponding to different stages of decomposition are given in Figure 2. Nb-rich regions have a higher atomic number than the Zr-rich matrix and appear brighter in the HAADF images. As can be seen, instead of showing uniform contrast/brightness, the original β phase regions (Nb-enriched) in samples 2.5Nb-1 and 2, Figure 2 (d and e), show a complex, fine-scale phase separated microstructure as a result of this partial decomposition. The wider contrast range in the 185-day sample (2.5Nb-2, Figure 2 e) suggests a higher enrichment of Nb in the remaining β-phase compared to the as-received state, showing evidence of reaching a later stage of the decomposition process. More significant microstructural changes are observed in the 2858-day sample, Figure 2 (c and f). After this much longer time, there are two characteristic morphologies of the Nb-enriched phases in the decomposed regions: small discrete precipitates of diameter ~20-50 nm, and more continuous Nb-rich phases at grain or the original interphase boundaries.

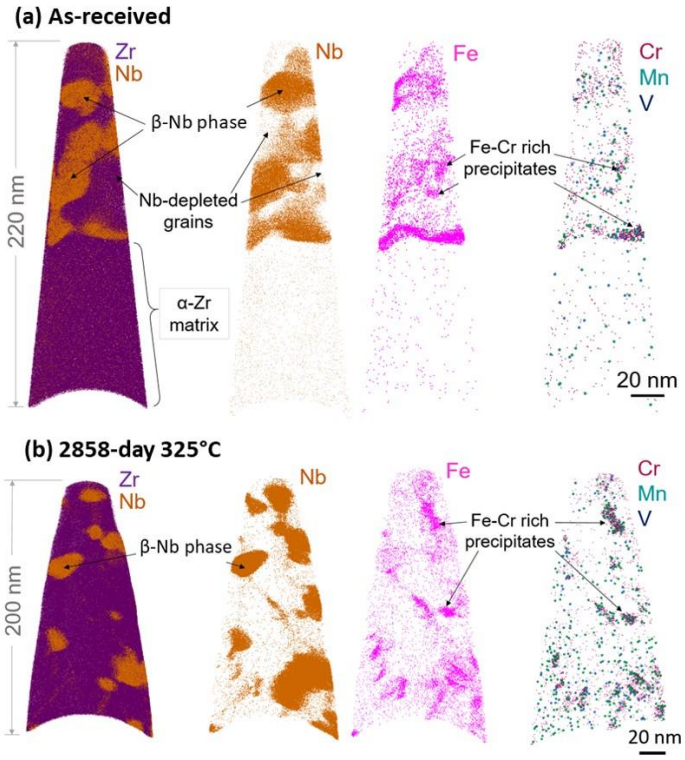

Figure 3 Reconstruction of 3D APT data showing the different morphologies of Nb-enriched β-Nb grains in the metal matrix of samples (a) 2.5Nb-1 and (b) 2.5Nb-3.

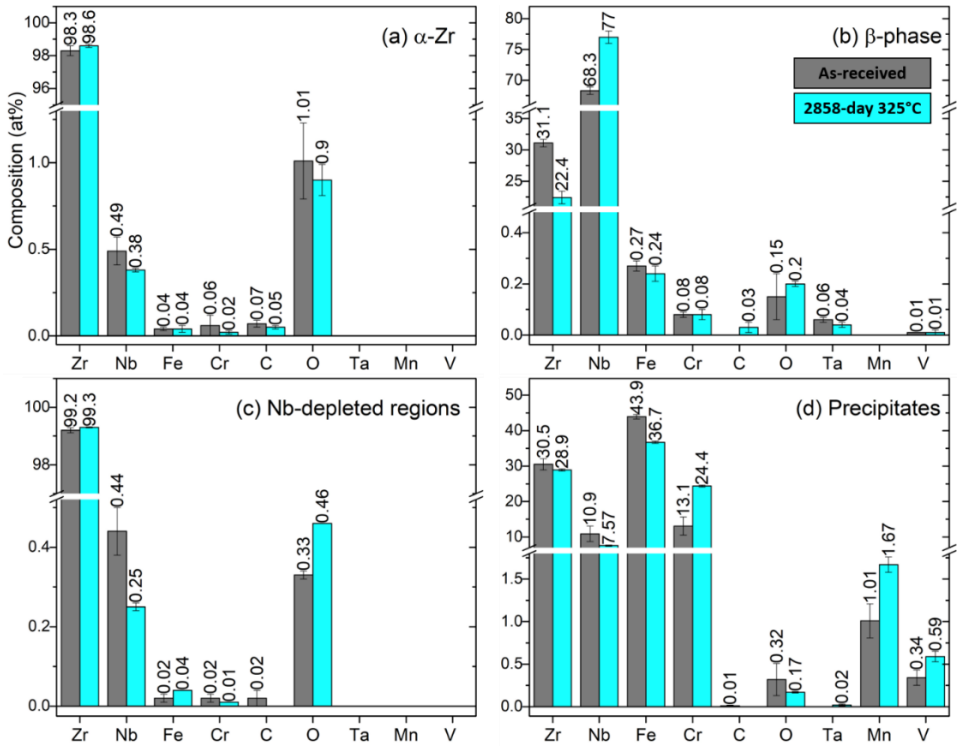

Figure 4 Average composition (at%) from APT data of different microstructural features in the metal matrix of 2.5Nb-1 (as-received) and 2.5Nb-3 (2858-day) samples. Composition values are shown on the top of the corresponding columns.

Due to the small scale of the features in both the as-received and thermally decomposed samples it was difficult in the TEM to make a quantitative analysis of their chemical compositions without interference from the surrounding α-Zr. APT was thus used to identify the chemical composition of these phases at the atomic scale. The 3D reconstructed APT data in Figure 3 was obtained from regions of decomposed β-Zr in samples in the as-received state and exposed to 325°C heavy water for 2858 days. Four regions can be recognised in the partially decomposed region in the as-received sample (2.5Nb-1); the α-Zr matrix, a strongly Nb-enriched phase, Nb-depleted grains within what was originally a β-Zr lath, and small precipitates rich in Cr and Fe, Figure 3 (a). A similar distribution of highly Nb-enriched particles and small precipitates can be seen in the long-term aged sample (2.5Nb-3), Figure 3 (b). The average chemical compositions for these features are compared for samples 2.5Nb-1 and 2.5Nb-3 in Figure 4.

Niobium has a very low solubility in the α-Zr phase [31], and by studying the formation of second phase particles in Zr–Nb alloys with Nb contents ranging from 0.10 to 0.86 wt%, Woo

and Griffiths [38] postulate that the solubility limit for Nb in a binary Zr-Nb alloy should lie between 0.29 wt% and 0.49 wt%. This is close to our direct APT measurements showing that the Nb concentration in the α-Zr matrix in the as-received Zr-2.5Nb samples is ~0.49 at%, Figure 4 (a). After long-term annealing, the Nb concentration in the α-Zr matrix reduces to 0.38 at% in sample 2.5Nb-3. The concentration of Nb in solid solution in the α matrix has been the parameter increasingly used to explain the effect of matrix chemistry changes on the overall corrosion rates of Zr alloys [6,39]. Urbanic and Griffiths [14] studied the corrosion performance of binary Zr-Nb alloys containing 0.02 to 1.35 wt% Nb and reported that the optimum corrosion resistance occurs at a Nb concentration in the α-matrix of about 0.1 wt%. More recently, Couet et al. [40] developed the Coupled Current Charge Compensation (C4) model, and suggested that the concentration of Nb in solid solution in the oxide can by aliovalent doping affect the overall corrosion kinetics of Zr-Nb alloys by changing the space charge generated [39]. The reduction in Nb in solid solution in the metal matrix as a result of long term annealing in our data will result in less Nb at higher charge states in the oxide being available to compensate for the build up in space charge, which is expected to contribute to a reduction in the corrosion rate of this Zr-2.5Nb alloy according to the C4 model [40,41].

The β-Zr grains formed during the extrusion process (at 815°C) should initially contain about 20 at% Nb, corresponding to the equilibrium composition defined by the monotectoid in the Zr-Nb phase diagram [31]. The final stress-relief treatment (400 °C for 24 h) and pre-filming process (400°C for 24 h) have already started the decomposition process of this β-Zr [35,37], and our APT results show phase separation to form particles with a Nb concentration of ~68 at%, Figure 4 (b). In order to identify the crystal structure of these Nb-rich regions, nanobeam diffraction patterns were indexed as having the bcc structure characteristic of β-Nb, as shown in Figure 5. This allows us to be confident that these Nb-rich features have, at a rather early stage of the decomposition process, already transformed to the equilibrium β-Nb phase, rather than the starting β-Zr or intermediate ω-Zr phases.

Long annealing allowed further decomposition of the initial β-Zr regions, leading to an increased Nb enrichment in the β-Nb grains to ~77 at% Nb, very close to the equilibrium

composition of this phase [31], Figure 4 (b), and these Nb-rich precipitates take on isolated, roughly spherical shapes, Figure 3 (b). Local composition analysis carried out on the APT data in regions surrounding these particles shows a Nb concentration even lower than that of the bulk α-Zr matrix, and these regions are thus defined as Nb-depleted regions in Figure 3 and 4. For example, in the as-received sample, the Nb content in these Nb-depleted regions is ~0.44 at%, and decreased to ~0.25 at% after 2858 days at 325°C.

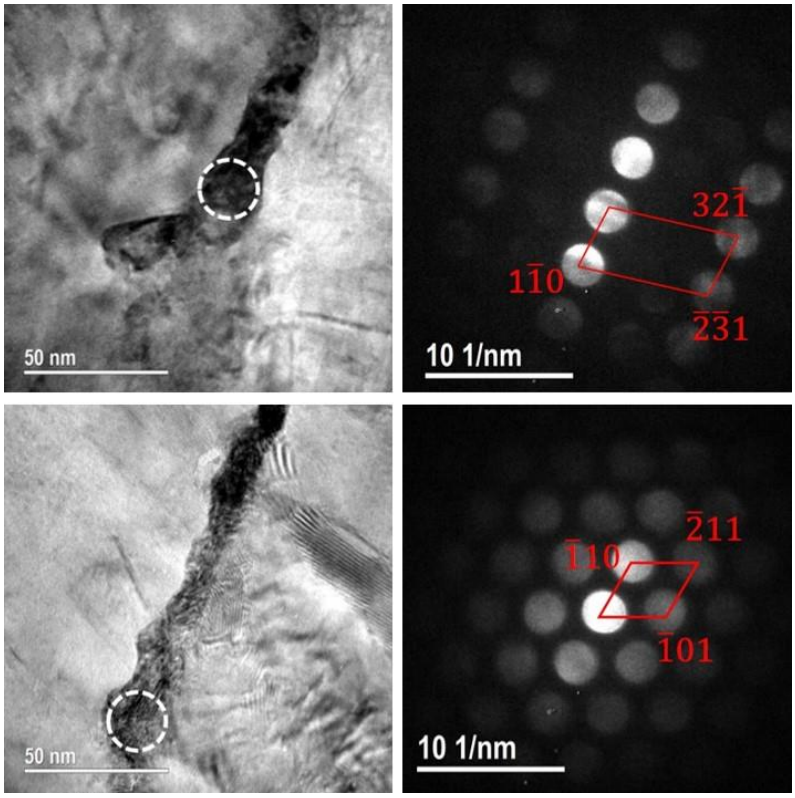

Figure 5 Bright field TEM images and nano beam diffraction analysis of two Nb-enriched regions in the metal matrix in sample 2.5Nb-2 (185 days at 325°C). The white circles in the left-hand images represent the positions of the focussed electron beam spot from where the diffraction patterns on the right were taken.

The APT data could also be used to study the distributions of the impurity elements like, Fe and O, as well as trace elements like Cr, Mn and V which are challenging to detect by EDX analysis. Oxygen is an α-stabiliser [37] and is observed mainly distributed within the α-Zr matrix, Figure 4 (a). Fe and Cr are β-stabilisers [37], but they are both rapid diffusers during the heat treatment involved in the manufacturing processes, and are observed in the as-received material to be segregated into fine precipitates at the α/β interphase boundaries, Figure 3 (a).

The formation of Cr- and Fe-rich Laves phase precipitates during the decomposition of the original β-Zr filaments has been reported previously [15,37], and although the crystal structure of these small Cr- and Fe-rich precipitates was not determined here, the average concentration from the APT analysis is close to the $Zr(Nb,Fe,Cr)_2$ Laves phase [42,43] and does not change significantly even after 2858-days at 325°C, Figure 4 (d).

3.3. Characterisation of oxide layers on the Zr-2.5Nb alloy

3.3.1. Oxide porosity and texture

The results of earlier works [21,44,45] suggest that alloys with better corrosion resistance generally have oxides with lower densities of cracks and fine porosity. Figure 6 shows the distribution of cracks and porosity in the oxide on the sample 2.5Nb-2. The high density of interconnected micro-cracks and nano-porosity, Figure 6 (b and c), in the outer oxide layer enable the direct ingress of coolant water so this outer oxide layer has lost all its protective character. When viewed along the TD, the larger cracks are roughly parallel to the sample surface, and their appearance roughly matches the locations of the original, but now decomposed and oxidised, β-Zr layers, Figure 6 (a and b). The size and distribution of cracks and porosity in the oxide grown on these Zr-2.5Nb samples are found to be very different to our previous observations on oxides on recrystallised ZIRLO, Zircaloy-4 and Zr-Nb samples [21,46–48]. On these alloys, the large cracks are roughly periodic and linked to the cyclic nature of the corrosion kinetics [48–50], and show a wave-like shape due to the large compressive stresses created by the volume expansion during oxidation of the zirconium metal. Careful study of these oxides has shown that the only region free of porosity (or containing a low density of mostly unconnected nanopores) is the inner oxide layer, the so-called barrier layer [46]. By comparison, Zr-2.5Nb alloy studied here shows a relatively better resistance to both corrosion and hydrogen pick-up [45], and although they are not corroded under exactly the same conditions, it is interesting to consider the effect of the different alloy microstructure on the oxide structure and chemistry. More specifically, the layered structure shown in Figure 1 will generate a characteristic oxide structure with narrow Nb-rich regions through which oxidising

species must penetrate to reach the underlying metal matrix. The TEM analysis in Figure 6 shows that the oxide regions immediately below the decomposed β-Zr layers are more compact and containing a much lower density of nanoscale porosity than the oxide structures studied in [46,47]. We now consider how this different morphology and distribution of cracks and porosity in the oxide may be controlled by the oxide growth through this layered microstructure.

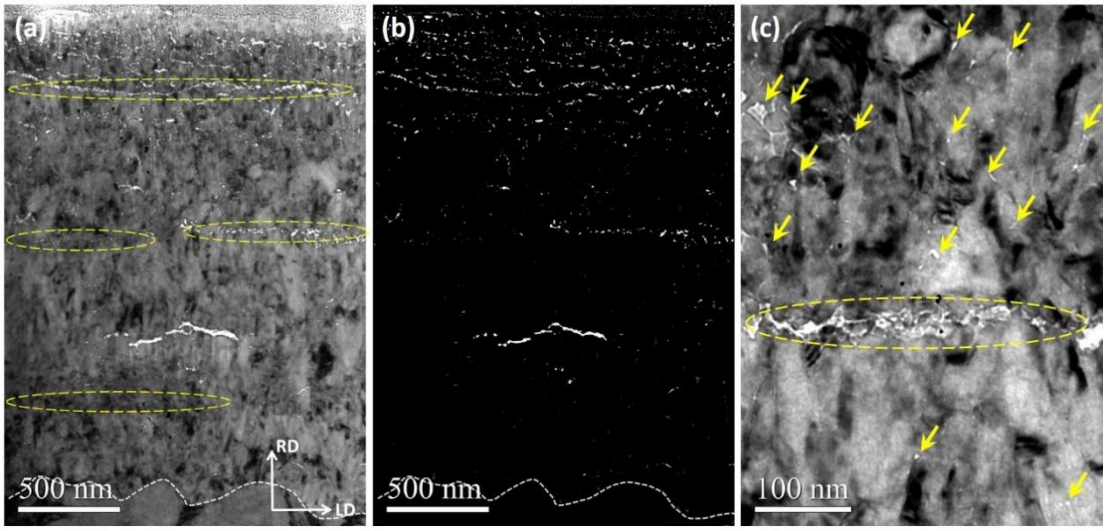

Figure 6 (a) Bright-field TEM images showing the overall oxide structure on the sample 2.5Nb-2, (b) detection of oxide cracks and nano-porosity using fast Fourier transform bandpass filter on the image in (a). (c) a high-magnification Fresnel contrast (Δf= -4000 nm) TEM image showing the oxide cracks and nano-porosity near the oxide of a decomposed β-Zr region. The oxide/metal interfaces are indicated by dashed lines, and examples of arrays of lateral cracks at previous β-Zr phase regions by yellow ellipses. The yellow arrows in (c) show examples of nano-pores.

A typical HAADF-STEM image and TKD maps from a similar region on the sample 2.5Nb-2 are shown in Figure 7. The contrast in HAADF imaging is sensitive to local variations of average atomic number, so the Nb-rich decomposed β-Zr layers near the oxide/metal interface appears brighter than the surrounding ZrO_2, as highlighted by the arrows in Figure 7 (a) because they are not yet fully oxidised. The delayed oxidation of Nb-rich phases as they become incorporated into the growing oxide has previously been reported in other alloys [51–53]. The Nb-rich regions that have been exposed in the oxide for a longer time (further from the oxide/metal interface), gradually become more fully oxidised and show similar intensity to the surrounding oxide, but their location can easily be recognised by the dense arrays of small lateral cracks generated in these regions. For instance, two layers of lateral cracks formed along

the original β-Zr phase lath can be seen about 1500 nm above the metal/oxide interface in the upper part of Figure 7 (a), and two more not yet fully oxidised about 500 nm above the interface. The band contrast map in Figure 7 (b) shows that the oxide grains formed on this Zr-2.5Nb alloy have a similar morphology to those previously reported on recrystallised Zircaloy-4 and Zr-Nb alloys [28,54], mostly well aligned columnar grains with a few small equiaxed grains.

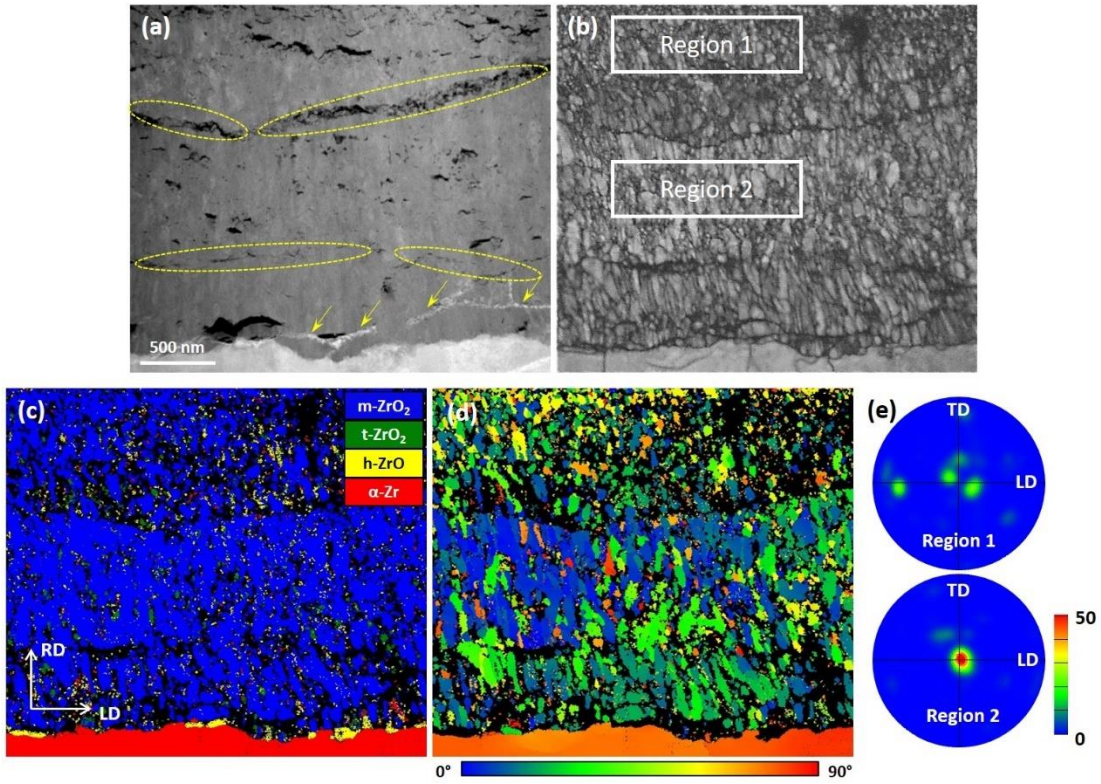

Figure 7 (a) HAADF-STEM image and (b, c and d) TKD maps of the same region showing the oxide microstructure on Sample 2.5Nb-2, (b) band contrast, (c) phase map and (d) texture component map. The grains in the texture component maps (d) are coloured according to the angular deviation of their $(10\bar{4})_{m\text{-}ZrO2}$ poles from the RD, (e) Contoured $(10\bar{4})_{m\text{-}ZrO2}$ poles (half width 10°) of m-ZrO_2 grains in regions 1 and 2 marked in (b) viewed along the RD. The yellow ellipses and arrows in (a) show the positions of original β-Zr laths that have decomposed and been oxidised to different degrees depending on the time they have spent in the oxide.

As often reported for oxides on other Zr alloys [54–57], most of the oxide grains are indexed as monoclinic ZrO_2 (m-ZrO_2), a small volume fraction of tetragonal ZrO_2 (t-ZrO_2) grains are found scattered throughout the oxide layers, and a thin discontinuous layer of plate-like hexagonal ZrO suboxide (h-ZrO) grains exists between the ZrO_2 and the α-Zr substrate, Figure 7 (c). The texture component map in Figure 7 (d) is coloured according to the orientation

deviation of oxide grains away from the $(10\bar{4})_{m\text{-}ZrO2}$‖RD fibre component. The results indicate that more than 50% of m-ZrO_2 grains through the oxide thickness are observed with $(10\bar{4})_{m\text{-}ZrO2}$ planes lying within 30° of the surface normal. However, the oxide texture observed on recrystallised Zircaloy-4 and Zr-Nb alloys [28,54] is stronger in the outer few microns of the oxide and decreases in strength towards the oxide/metal interface, while in this Zr-2.5Nb sample the sharpness of the oxide texture changes periodically. Once the oxide grows past each of the original β-Zr layers there is a sharp change in the texture strength, and below the β layers the $(10\bar{4})_{m\text{-}ZrO2}$ texture of the oxide is once again better aligned with the surface normal, Figure 7 (d and e). Previous studies [28,58] show that the substrate orientation does not significantly affect oxide texture development, and the main driving force for oxide texture development is oxidation-induced stress [59]. We suppose that the increase in oxide texture strength observed beneath the β layers is a result of the transiently slower corrosion rate as the growth front passes the β layer, which thus allows time for the nucleation and growth of well-orientated columnar grains.

The HAADF image in Figure 8 also shows that these Nb-rich layers at which the oxide texture changes also control the local oxidation rate of the underlying metal matrix. The oxide front is blocked by the slower oxidation of the Nb-rich layer on the left hand side of the image, but has consumed an extra 100 nm of metal matrix on the right hand side. The observation of a sharper oxide texture under each Nb-rich layer suggests that the oxide grains are re-nucleated every time the oxide front passes one of these strips of original β-Zr. This layer of freshly nucleated grains will have the characteristics of the columnar regions observed on almost all alloys at the early stages of corrosion; increased cohesion between grains and reduced porosity, and a predominance of low-angle grain boundaries offering only low mobility paths for diffusing species. Combining these observations, we can see how the alloy microstructure can affect the local oxidation rate in two ways; the delayed oxidation of the Nb-rich regions themselves (Figure 8) and modified nucleation and growth process under these regions (Figure 7) which develops a more compact and stronger textured oxide structure and can therefore result in the improved corrosion resistance.

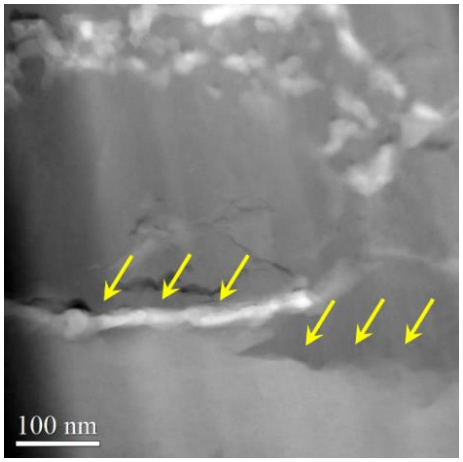

Figure 8 HAADF image showing the oxide/metal interface in Sample 2.5Nb-3 (2858 days at 325°C). The yellow arrows indicate the interface positions. The oxide layer is darker in the HAADF mode because it has a lower average atomic mass compared to the metal matrix, and the heavier residual Nb-rich regions also show brighter intensity.

3.3.2. Oxidation of the β-Zr phase

The different stages of decomposition of the original β-Zr layers described above may also result in different oxidation behaviour as they are incorporated into a growing oxide. As discussed above, the final stress-relief treatment (400°C for 24 h) has partially decomposed the β-Zr into the complex fragmented internal structure as shown in Figure 2 and 3, and most of the original β-phase has already decomposed into fine β-Nb particles surrounded by Nb depleted regions of α-Zr. These β-Nb particles should oxidise more slowly than the α-Zr matrix [51,53], and when they are incorporated into the oxide, small cracks will form on top of each particle as described for second phase particles in recrystallized Zr alloys [48,50]. If the local concentration of small β-Nb particles is high, as it will be due to the decomposition of a lath of β-Zr, a connected network of nanoscale porosity will form at the site of the original lath, Figure 9 (a). Long exposure to the 'corrosion' temperatures encourages the metastable β phases to further decompose, forming larger discrete β-Nb particles or continuous β-Nb layers, Figure 2, 3 and 4. When these long-term thermally decomposed Nb-rich phases are incorporated into the oxide, instead of the formation of a network of small cracks, larger lateral cracks are found on the top of these larger β-Nb particles, Figure 9. These different distributions of cracks and porosity as a result of the progressively changing microstructure of the original β-Zr laths may thus play an important role in determining the local corrosion rate. More generally, the

existence of small, discrete β-Nb precipitates in most Nb-containing alloys compared to the characteristic continuous β-Zr layers in the alloy studied here could have a major influence on both the shape and the density of cracks and porosity when the β phases are oxidised.

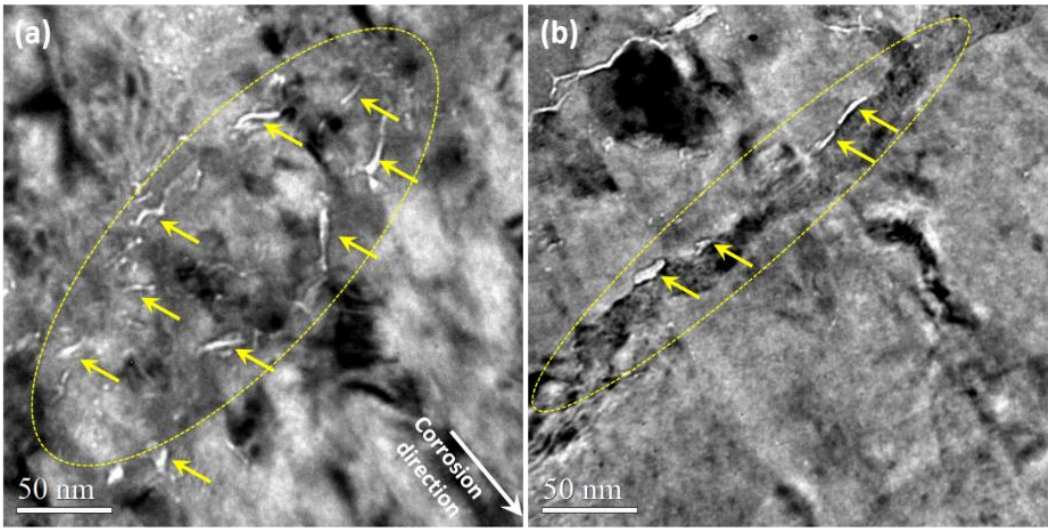

Figure 9 Typical Fresnel contrast (Δf= -4000 nm) TEM images showing the porosity around oxidised β phase regions in the oxides on sample (a) 2.5Nb-2, 185 days at 325°C and (b) 2.5Nb-3, 2858 days at 325°C. The yellow ellipses show the regions of decomposed and oxidised β-Zr. Some small cracks and nano porosity are marked by the yellow arrows.

3.3.3.Oxide/metal interface morphology

Recent studies on other Zr alloys [44,60] have shown that the combined thickness of the h-ZrO suboxide and oxygen-saturated layers at the oxide/metal interface correlate well to the instantaneous oxidation rate, suggesting that this oxygen-rich zone is part of the protective oxide that is rate limiting in the transport processes involved in oxidation. Figure 10 shows MLLS fitting coefficients maps of low-loss EELS spectra acquired from a 185-day corroded Zr-2.5Nb sample (2.5Nb-2) to reveal the location and thickness of suboxide and oxygen-saturated layers. Figure 10 (a) is the coefficient map for ZrO_2, in which the oxide shows brightest contrast, the suboxide grey contrast, and the metal matrix dark contrast. Instead of the sawtooth-like suboxide grains normally observed on the recrystallized Zircaloy-4 and Zr-Nb alloys [28], the suboxide grains on this Zr-2.5Nb alloy are more plate-like in shape, Figure 7 and 10. Because of the previously analysed preferred orientation relationship between the suboxide and underlying metal [28], this is likely to be a result of the different underlying α-Zr grain orientations (crystalline texture) in this material. The recrystallized Zircaloy-4 and Zr-Nb

alloys have their basal [0002] poles close to the radial direction [17,58], while the Zr-2.5Nb alloy in this study has its [0002] poles close to the transverse direction. The h-ZrO suboxide layers on this Zr-2.5Nb alloy are also observed to be much thinner than those on recrystallised Zr alloys [28] at all corrosion times.

The formation of the metastable h-ZrO suboxide requires high levels of local stress [28,61] generated by the volume expansion on forming the oxide, and the thinner suboxide layers observed may suggest that the local stresses generated during the corrosion process are limited on this Zr-2.5Nb alloy compared to recrystallised Zr alloys. Results from finite element modelling [62] predict that the stresses accumulated at the oxide/metal interface during the oxidation of Zr alloys are highly sensitive to the interface roughness, and that when the interface undulation amplitude decreases from 0.2 μm to 0.05 μm, the tensile hoop stress in the metal matrix decreases from ~ 2 GPa to ~ 0.3 GPa, and the tensile radial stress from ~ 2.4 GPa to ~ 0.5 GPa. In our recent work [45] we have shown that the average roughness of the oxide/metal interface on this Zr-2.5Nb alloy is much smaller than that on recrystalised Zircaloy-4 samples even after 2000-days of aqueous corrosion. The thinner suboxide layers observed on this Zr-2.5Nb alloy may also suggest that any stresses generated during oxidation are released more easily than in the alloys more commonly used for PWR cladding tubes. The Zr-2.5Nb alloy studied here consists of elongated α-Zr grains and thin layers of partially decomposed Nb-rich β-Zr, while recrystallised alloys like Zircaloy-4 or M5 alloys show equiaxed α-Zr grains and uniformly distributed second phase particles. These different microstructure will inevitably lead to variations in the mechanical properties. For example, the yield strength of tubes of a Zr-2.5Nb alloy similar to that studied in this paper is around 600 MPa at 300°C along the tangential direction [63], ~ 2.5 times higher than that measured in recrystallised Zircaloy-4 or M5 alloys [64].

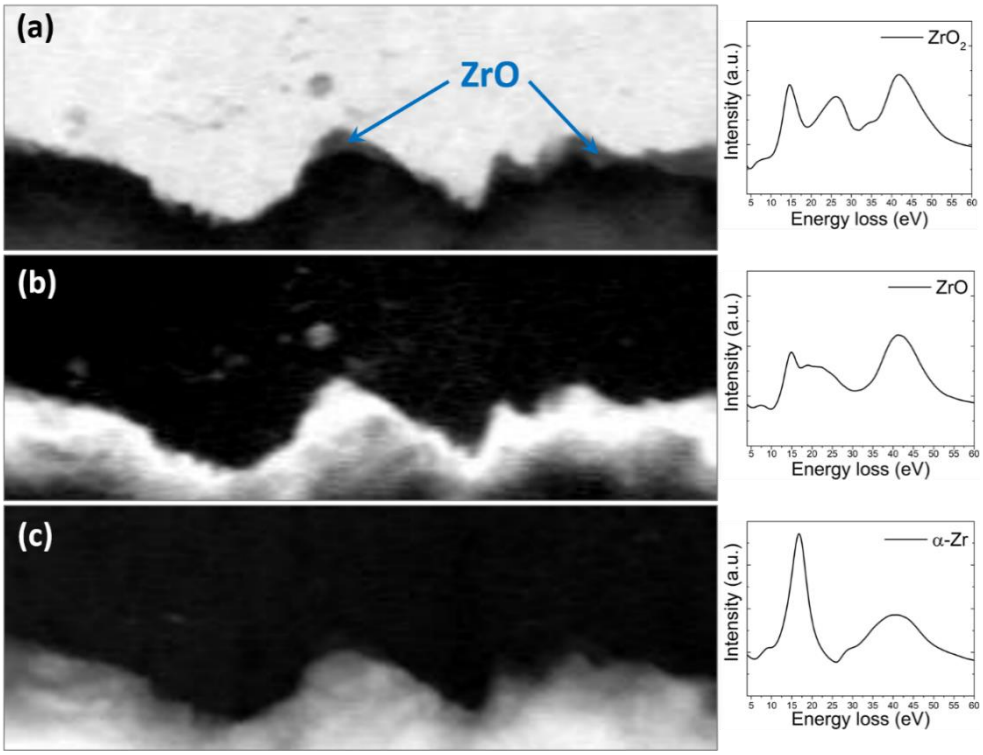

Figure 10 EELS fitting coefficient maps showing the phase distribution at the oxide/metal interface on sample 2.5Nb-2. The brighter contrast indicates higher fitting coefficient for the selected fitting reference, (a) ZrO_2, (b) ZrO suboxide and oxygen-saturated metal matrix and (c) metal matrix. The ZrO suboxide grains in (a) show intermediate gray contrast.

3.3.4.Li transportation through the oxide layers on the Zr-2.5Nb alloy

LiOH is added to the primary coolant (D_2O) of the samples studied here to maintain a slightly alkaline or neutral pH value. Previous work has shown that adding LiOH will normally degrade the corrosion performance of Zircaloy-2, Zircaloy-4 and Zr-2.5Nb alloys [65–68], but the Zr-2.5Nb alloy shows different lithium accelerated corrosion behaviour compared to Zircaloy-4 [65,67] , possibly as a result of the different morphologies and distributions of second phases in the metal matrix and oxide layers. There has been little direct experimental evidence to show how Li interacts with the Nb-rich layers during corrosion in lithiated solutions. In this study, a Cameca NanoSIMS 50L with a RF plasma oxygen source was used to measure $^{7}Li^{+}$ and $^{93}Nb^{+}$ signals simultaneously. Figure 11 (a-c) shows the cross-sectional views from high-resolution SIMS mapping of the $^{7}Li^{+}$ and $^{93}Nb^{+}$ signals from the oxide layer on a 700-day corroded Zr-2.5Nb sample (2.5Nb-4). We can see a direct correlation between the high $^{93}Nb^{+}$ signal at the initial locations of the β-Zr layers, and the $^{7}Li^{+}$ signal, and also less evidence of trapped Li in the Nb-rich regions within the inner oxide layer. Using the observations above on the local

nanocracking and porosity around the original β-Zr layers as they oxidise (Figures 6 and 9), and the dense, columnar nature of the re-nucleated oxide grains under each layer (Figure 7 d), we can interpret the SIMS results as suggesting that the decomposed β-Zr regions are preferentially trapping Li species and the dense inner oxide layers act as barriers to inward diffusion. Previous SIMS measurements on Zircaloy-4 show rather similar results for the gradual decrease in Li content closer to the metal/oxide interface [69], but did not have the lateral and depth resolution to determine the correlation with the original metal microstructure. We also note that 3D SIMS experiments on the distribution of deuterium in the same Zr-2.5Nb alloys [45] show that the deuterium is not preferentially trapped in the decomposed β-Zr regions, but that these Nb-rich layers do act as effective barriers to inward diffusion. Combining these results adds weight to the idea that the Nb-rich β-Zr layers can be effective barriers to oxidising species during the aqueous corrosion of these Zr-2.5Nb alloy, and contribute to their improved corrosion resistance when compared to recrystalized Zircaloy-2 and Zircaloy-4 alloys.

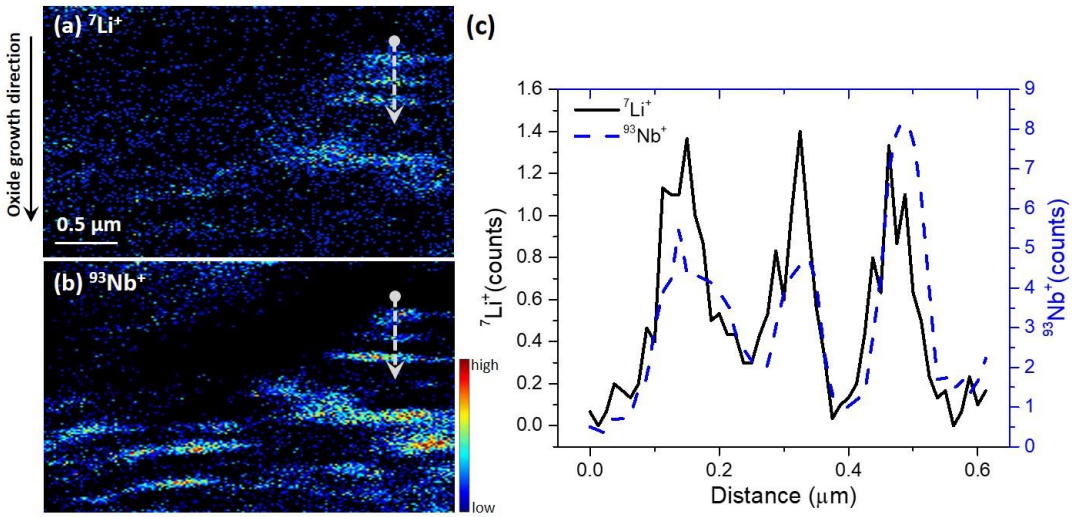

Figure 11 Cross-sectional views of the 3D NanoSIMS data from the oxides layers on a 700-day autoclave-corroded Zr-2.5Nb sample (2.5Nb-4) showing the distributions of (a) $^{7}Li^{+}$, (b) $^{93}Nb^{+}$ and (c) line scans along the lines marked in (a) and (b)

Conclusions

We used a range of advanced microscopy techniques to study the decomposition behaviour of metastable β-Zr phases in a Zr-2.5Nb alloy under reactor coolant loop conditions. The key findings include:

1) The β-Zr layers in the original microstructure are heavily decomposed even after the short stress stage at 400°C at the end of the manufacturing cycle, with a closely packed array of β-Nb precipitates forming in an α-Zr matrix. The Nb content of these precipitates gradually increases to 77 at% after 2858 days at 325ºC, and the local matrix concentration decreases from 0.44 to 0.25 at%. Over the same long periods at elevated temperature the β-Nb precipitates coarsen to some extent and become better defined, but there is still an intimate mixture of fine β-Nb and Nb-depleted α-Zr. This process is illustrated schematically in Figure 12. It is these bands of multi-phase microstructure (with small Cr and Fe-rich precipitates) through which the oxidation front must progress during the corrosion process – a very different structure than the dispersed Nb-rich SPP population in recrystallised alloys.
2) As a result of this gradual decomposition, the precise structure of the oxide formed by the consumption of each Nb-rich band will depend on when the oxidation front reaches it, and so how long it has spent in the metal matrix.
3) We have shown that the oxidation of these bands is significantly slower than the surrounding α-Zr matrix, and also that the oxidation of the very dense array of small β-Nb precipitates results in a high density of small cracks and pores where Li from the water chemistry is preferentially trapped.
4) Under these bands, the TKD analysis shows that the zirconium oxide is re-nucleated to generate a characteristic dense array of new columnar grains, and the combination of the Nb-rich remnants of the original β-Zr layers and this new dense oxide is an effective barrier to both deuterium and lithium penetration.

These new observations show how this improved corrosion performance of the Zr-2.5Nb alloy is achieved by a detailed analysis of the decomposition and oxidation behaviour of the β-Zr and the effect of its characteristic layered morphology. We conclude that the original layered microstructure of this Zr-2.5Nb alloy plays an important role in determining their corrosion performance since each band of decomposed β-Zr offers a significant barrier to the oxidation front (and also to the penetration of hydrogenic species). This characteristic microstructure is

controlled by the metallurgical history of the alloys – especially the hot extrusion and drawing stages. In the design of future Zr alloys with better corrosion resistance, it is proposed that fabrication processes or thermal heat treatment conditions need to be adjusted so that the metastable β-Zr layers can further decompose before service to generate a microstructure with uniform and continuous β-Nb layers.

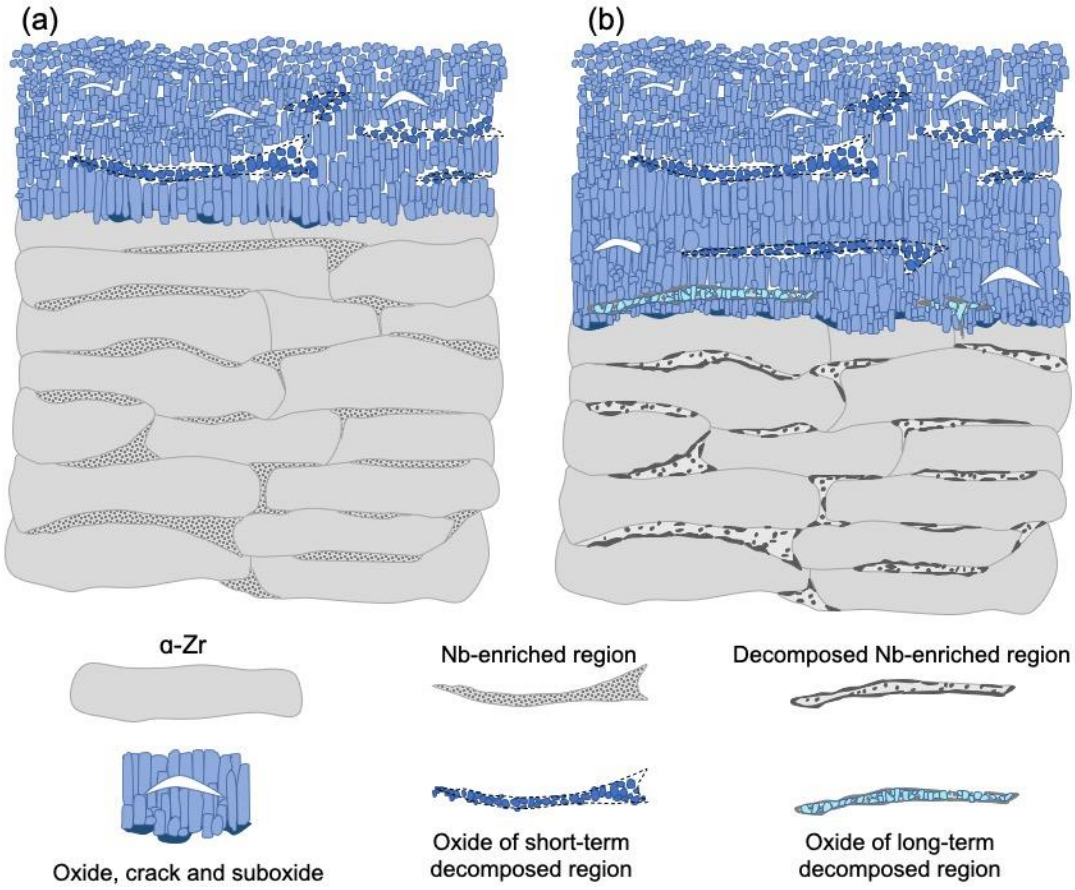

Figure 12 Schematic representations of the microstructures of the oxides and metal matrix of (a) short term corroded and (b) long term thermally decomposed and corroded Zr-2.5Nb.

Acknowledgements

The authors acknowledge the contribution made to this work by their collaborators from the MUZIC project. Support for work on active samples was provided by EPSRC grant (EP/M018237/1). Some of the work on radioactive samples was done using UKAEA's Materials Research Facility (MRF), which has been funded by the UK's National Nuclear User Facility (NNUF) and Henry Royce Institute initiative. EPSRC grants (EP/K040375/1 and

EP/N010868/1) are acknowledged for funding the ‘South of England Analytical Electron Microscope’ and the Zeiss Crossbeam and Nvision FIB/SEM used in this research. The NanoSIMS 50L was funded by UK Research Partnership Investment Funding (UKRPIF) Manchester RPIF Round 2. This work was supported by the Henry Royce Institute for Advanced Materials, funded through EPSRC grants EP/R00661X/1, EP/S019367/1, EP/P025021/1 and EP/P025498/1. JL would acknowledge the EPSRC grants EP/P001645/1 and EP/R006245/1. GH is grateful for the support from EPSRC grant EP/R511742/1.

Reference

[1] C.R.F. Azevedo, Selection of fuel cladding material for nuclear fission reactors, Engineering Failure Analysis. 18 (2011) 1943–1962. https://doi.org/10.1016/j.engfailanal.2011.06.010.

[2] L. Hallstadius, S. Johnson, E. Lahoda, Cladding for high performance fuel, Progress in Nuclear Energy. 57 (2012) 71–76. https://doi.org/10.1016/j.pnucene.2011.10.008.

[3] A.T. Motta, A. Couet, R.J. Comstock, Corrosion of Zirconium Alloys Used for Nuclear Fuel Cladding, Annual Review of Materials Research. 45 (2015) 311–343. https://doi.org/10.1146/annurev-matsci-070214-020951.

[4] A. V. Nikulina, Zirconium-Niobium Alloys for Core Elements of Pressurized Water Reactors, Metal Science and Heat Treatment. 45 (2003) 287–292. https://doi.org/10.1023/A:1027388503837.

[5] J.-P. Mardon, D. Charquet, J. Senevat, Influence of Composition and Fabrication Process on Out-of-Pile and In-Pile Properties of M5 Alloy, in: Zirconium in the Nuclear Industry: Twelfth International Symposium, ASTM International, 100 Barr Harbor Drive, PO Box C700, West Conshohocken, PA 19428-2959, 2000: pp. 505-524. https://doi.org/10.1520/STP14314S.

[6] Y.H. Jeong, H.G. Kim, T.H. Kim, Effect of β phase, precipitate and Nb-concentration in matrix on corrosion and oxide characteristics of Zr–xNb alloys, Journal of Nuclear Materials. 317 (2003) 1–12. https://doi.org/10.1016/S0022-3115(02)01676-8.

[7] G. Pan, A.M. Garde, A.R. Atwood, Performance and Property Evaluation of High-Burnup Optimized ZIRLOTM Cladding, in: R.J. Comstock, P. Barberis (Eds.), Zirconium in the Nuclear Industry: 17th Volume, 2015: pp. 607–627. https://doi.org/10.1520/STP154320130008.

[8] B.A. Cheadle, The Development of Zr-2.5Nb Pressure Tubes for CANDU Reactors, in: Zirconium in the Nuclear Industry: 16th International Symposium, ASTM International, 2010: pp. 67–87. https://doi.org/10.1520/stp152920120004.

[9] V. Perovic, A. Perovic, G.C.C. Weatherly, L.M.M. Brown, G.R.R. Purdy, R.G.G. Fleck, R.A.A. Holt, Microstructural and microchemical studies of Zr-2.5Nb pressure tube alloy, Journal of Nuclear Materials. 205 (1993) 251–257. https://doi.org/10.1016/0022-3115(93)90087-F.

[10] H. Yu, K. Zhang, Z. Yao, M.A. Kirk, F. Long, M.R. Daymond, Metastable phases in Zr-Excel alloy and their stability under heavy ion (Kr^{2+}) irradiation, Journal of Nuclear Materials. 469 (2016) 9–19. https://doi.org/10.1016/j.jnucmat.2015.11.020.

[11] Y.H. Jeong, H.G. Kim, D.J. Kim, B.K. Choi, J.H. Kim, Influence of Nb concentration in the α-matrix on the corrosion behavior of Zr-xNb binary alloys, Journal of Nuclear Materials. 323 (2003) 72–80. https://doi.org/10.1016/j.jnucmat.2003.08.031.

[12] Y.P. Lin, O.T. Woo, Oxidation of β-Zr and related phases in Zr–Nb alloys: an electron microscopy investigation, Journal of Nuclear Materials. 277 (2000) 11–27. https://doi.org/10.1016/S0022-3115(99)00153-1.

[13] G.M. McDougall, V.F. Urbanic, The Influence of Material Variables on Corrosion and Deuterium Uptake of Zr-2.5Nb Alloy During Irradiation, in: G.D. Moan, P. Rudling (Eds.), Zirconium in the Nuclear Industry: Thirteenth International Symposium, ASTM International, West Conshohocken, PA, 2002: pp. 247–273. https://doi.org/10.1520/STP11392S.

[14] V. Urbanic, M. Griffiths, Microstructural Aspects of Corrosion and Hydrogen Ingress in Zr-2.5Nb, in: Zirconium in the Nuclear Industry: Twelfth International Symposium, ASTM International, 100 Barr Harbor Drive, PO Box C700, West Conshohocken, PA 19428-2959, 2000: pp. 641–658. https://doi.org/10.1520/STP14321S.

[15] D.O. Northwood, X. Meng-Burany, X. Meng-Burany, B.D. Warr, Microstructure of Zr-2.5Nb Alloy Pressure Tubing, in: C.M. Eucken, A.M. Garde (Eds.), Zirconium in the Nuclear Industry: Ninth International Symposium, ASTM International, West Conshohocken, PA, 1991: pp. 156–176. https://doi.org/10.1520/STP25506S.

[16] C.D. Judge, W. Li, C. Mayhew, A. Buyers, G.A. Bickel, Adopting Transmission Kikuchi Diffraction to Characterize Grain Structure and Texture of Zr-2.5Nb CANDU Pressure Tubes, CNL Nuclear Review. 7 (2017) 119–125. https://doi.org/10.12943/CNR.2017.00010.

[17] K.L. Murty, I. Charit, Texture development and anisotropic deformation of zircaloys, Progress in Nuclear Energy. 48 (2006) 325–359. https://doi.org/10.1016/j.pnucene.2005.09.011.

[18] J. Liu, High resolution structural analysis of irradiated zirconium alloys, DPhil thesis, University of Oxford, 2019.

[19] S. Lozano-Perez, A guide on FIB preparation of samples containing stress corrosion crack tips for TEM and atom-probe analysis, Micron. 39 (2008) 320–328. https://doi.org/10.1016/j.micron.2007.12.003.

[20] M.L. Jenkins, Characterisation of radiation-damage microstructures by TEM, Journal of Nuclear Materials. 216 (1994) 124–156. https://doi.org/10.1016/0022-3115(94)90010-8.

[21] N. Ni, S. Lozano-Perez, M.L. Jenkins, C. English, G.D.W. Smith, J.M. Sykes, C.R.M. Grovenor, Porosity in oxides on zirconium fuel cladding alloys, and its importance in controlling oxidation rates, Scripta Materialia. 62 (2010) 564–567. https://doi.org/10.1016/j.scriptamat.2009.12.043.

[22] S.J. Pennycook, P.D. Nellistt, Scanning Transmission Electron Microscopy: Imaging and Analysis, Springer Science & Business Media, 2011. https://doi.org/https://doi.org/10.1007/978-1-4419-7200-2.

[23] P. Longo, The use of MLLS fitting approach to resolve overlapping edges in the EELS spectrum at the atomic level | Gatan, Inc., (n.d.).

[24] T.F. Kelly, M.K. Miller, Atom probe tomography, Review of Scientific Instruments. 78 (2007) 31101. https://doi.org/10.1063/1.2709758.

[25] A. Harte, R.P. Babu, C.A. Hirst, T.L. Martin, P.A.J. Bagot, M.P. Moody, P. Frankel, J. Romero, L. Hallstadius, E.C. Darby, M. Preuss, Understanding irradiation-induced nanoprecipitation in zirconium alloys using parallel TEM and APT, Journal of Nuclear Materials. 510 (2018) 460–471. https://doi.org/10.1016/j.jnucmat.2018.08.033.

[26] T.F. Kelly, M.K. Miller, Atom probe tomography ARTICLES YOU MAY BE INTERESTED IN, (2007). https://doi.org/10.1063/1.2709758.

[27] J. Liu, S. Lozano-Perez, P. Karamched, J. Holter, A.J. Wilkinson, C.R.M. Grovenor, Forescattered electron imaging of nanoparticles in scanning electron microscopy, Materials Characterization. 155 (2019) 109814. https://doi.org/10.1016/j.matchar.2019.109814.

[28] J. Liu, H. Yu, P. Karamched, J. Hu, G. He, D. Goran, G.M. Hughes, A.J. Wilkinson, S. Lozano-Perez, C.R.M. Grovenor, Mechanism of the α-Zr to hexagonal-ZrO transformation and its impact on the corrosion performance of nuclear Zr alloys, Acta Materialia. 179 (2019) 328–341. https://doi.org/10.1016/j.actamat.2019.08.051.

[29] K. Li, T. Aarholt, J. Liu, H. Hulme, A. Garner, M. Preuss, S. Lozano-Perez, C. Grovenor, 3D-characterization of deuterium distributions in zirconium oxide scale using high-resolution SIMS, Applied Surface Science. 464 (2019) 311–320. https://doi.org/10.1016/j.apsusc.2018.09.101.

[30] Poczatek, C, Z. Kaufman, C. Lechene, OpenMIMS ImageJ Plugin Guide, (2012).

[31] J.P. Abriata, J.C. Bolcich, The Nb−Zr (Niobium−Zirconium) system, Journal of Phase Equilibria. 3 (1982) 34–44. https://doi.org/10.1007/BF02873409.

[32] J. Liu, S. Lozano-Perez, A.J. Wilkinson, C.R.M. Grovenor, On the depth resolution of transmission Kikuchi diffraction (TKD) analysis, Ultramicroscopy. 205 (2019) 5–12. https://doi.org/10.1016/j.ultramic.2019.06.003.

[33] G. Choudhuri, Jagannath, M. Kiran Kumar, V. Kain, D. Srivastava, S. Basu, B.K. Shah, N. Saibaba, G.K. Dey, Influence of Fe content on corrosion and hydrogen pick up behavior of Zr–2.5Nb pressure tube material, Journal of Nuclear Materials. 441 (2013) 178–189. https://doi.org/10.1016/J.JNUCMAT.2013.05.026.

[34] N. Saibaba, S. Jha, S. Tonpe, K. Vaibhaw, V. Deshmukh, S. Ramana Rao, K. Mani Krishna, S. Neogy, D. Srivastava, G. Dey, R. Kulkarni, B. Rath, E. Ramadasan, S. Anantharaman, Microstructural Studies of Heat Treated Zr-2.5Nb Alloy for Pressure Tube Applications, Journal of ASTM International. 8 (2011) 1–15. https://doi.org/10.1520/JAI103213.

[35] G. Choudhuri, D. Srivastava, K.R. Gurumurthy, B.K. Shah, Optimization of stress relief heat treatment of PHWR pressure tubes (Zr-2.5Nb alloy), Journal of Nuclear Materials. 383 (2008) 178–182. https://doi.org/10.1016/j.jnucmat.2008.08.058.

[36] M.T. Jovanović, R.L. Eadie, Y. Ma, M. Anderson, S. Sagat, V. Perović, The effect of annealing on hardness, microstructure and delayed hydride cracking in Zr-2.5Nb pressure tube material, Materials Characterization. 47 (2001) 259–268. https://doi.org/10.1016/S1044-5803(01)00179-6.

[37] M. Griffiths, J.E. Winegar, A. Buyers, The transformation behaviour of the β-phase in Zr–2.5Nb pressure tubes, Journal of Nuclear Materials. 383 (2008) 28–33. https://doi.org/10.1016/J.JNUCMAT.2008.08.003.

[38] O.T. Woo, M. Griffiths, The role of Fe on the solubility of Nb in α-Zr, Journal of Nuclear Materials. 384 (2009) 77–80. https://doi.org/10.1016/J.JNUCMAT.2008.10.004.

[39] M. Moorehead, Z. Yu, L. Borrel, J. Hu, Z. Cai, A. Couet, Comprehensive investigation of the role of Nb on the oxidation kinetics of Zr-Nb alloys, Corrosion Science. 155 (2019) 173–181. https://doi.org/10.1016/j.corsci.2019.04.017.

[40] A. Couet, A.T. Motta, A. Ambard, The coupled current charge compensation model for zirconium alloy fuel cladding oxidation: I. Parabolic oxidation of zirconium alloys, Corrosion Science. 100 (2015) 73–84. https://doi.org/10.1016/j.corsci.2015.07.003.

[41] Z. Yu, J.W. Werden, N.A. Capps, K.D. Linton, A. Couet, (S)TEM/EDS study of native precipitates and irradiation induced Nb-rich platelets in high-burnup M5®, Journal of Nuclear Materials. 544 (2021) 152667. https://doi.org/10.1016/j.jnucmat.2020.152667.

[42] B. Tao, R. Qiu, Y. Zhao, Y. Liu, X. Tan, B. Luan, Q. Liu, Effects of alloying elements (Sn, Cr and Cu) on second phase particles in Zr-Sn-Nb-Fe-(Cr, Cu) alloys, Journal of Alloys and Compounds. 748 (2018) 745–757. https://doi.org/10.1016/j.jallcom.2018.03.203.

[43] P. Barberis, C. Vauglin, P. Fremiot, P. Guerin, Thermodynamics of Zr Alloys: Application to Heterogeneous Materials, in: B. Comstock, P. Barberis (Eds.), Zirconium in the Nuclear Industry: 17th Volume, ASTM International, West Conshohocken, PA, 2015: pp. 1–20. https://doi.org/10.1520/STP154320120208.

[44] M. Preuss, P. Frankel, S. Lozano-Perez, D. Hudson, E. Polatidis, N. Ni, J. Wei, C. English, S. Storer, K.B. Chong, M. Fitzpatrick, P. Wang, J. Smith, C. Grovenor, G. Smith, J. Sykes, B. Cottis, S. Lyon, L. Hallstadius, B. Comstock, A. Ambard, M. Blat-Yrieix, P. Barberis, S.W. Dean, Studies Regarding Corrosion Mechanisms in Zirconium Alloys, Journal of ASTM International. 8 (2011) 103246. https://doi.org/10.1520/JAI103246.

[45] J. Liu, K. Li, J. Sayers, T. Aarholt, G. He, H. Hulme, A. Garner, M. Preuss, H. Nordin, J.M. Partezana, M. Limbäck, S. Lozano-Perez, S. Ortner, C.R.M. Grovenor, K. Moore, M. Preuss, H. Nordin, J.M. Partezana, M. Limbäck, S. Lozano-Perez, S. Ortner, C.R.M. Grovenor, Characterisation of deuterium distributions in corroded zirconium alloys

using high-resolution SIMS, Acta Materialia. 200 (2020) 581–596. https://doi.org/10.1016/j.actamat.2020.09.040.

[46] J. Hu, J. Liu, S. Lozano-Perez, C.R.M. Grovenor, M. Christensen, W. Wolf, E. Wimmer, E. v. Mader, Hydrogen pickup during oxidation in aqueous environments: The role of nano-pores and nano-pipes in zirconium oxide films, Acta Materialia. 180 (2019) 105–115. https://doi.org/10.1016/J.ACTAMAT.2019.09.005.

[47] A. Couet, L. Borrel, J. Liu, J. Hu, C. Grovenor, An integrated modeling and experimental approach to study hydrogen pickup mechanism in zirconium alloys, Corrosion Science. (2019) 108134. https://doi.org/10.1016/j.corsci.2019.108134.

[48] N. Ni, S. Lozano-Perez, J.M. Sykes, G.D.W. Smith, C.R.M. Grovenor, Focussed ion beam sectioning for the 3D characterisation of cracking in oxide scales formed on commercial ZIRLOTM alloys during corrosion in high temperature pressurised water, Corrosion Science. 53 (2011) 4073–4083. https://doi.org/10.1016/j.corsci.2011.08.013.

[49] B. de Gabory, A.T. Motta, K. Wang, Transmission electron microscopy characterization of Zircaloy-4 and ZIRLOTM oxide layers, Journal of Nuclear Materials. 456 (2015) 272–280. https://doi.org/10.1016/j.jnucmat.2014.09.073.

[50] P. Tejland, H.-O. Andrén, Origin and effect of lateral cracks in oxide scales formed on zirconium alloys, Journal of Nuclear Materials. 430 (2012) 64–71. https://doi.org/10.1016/j.jnucmat.2012.06.039.

[51] K. Sakamoto, K. Une, M. Aomi, T. Otsuka, K. Hashizume, Change of chemical states of niobium in the oxide layer of zirconium-niobium alloys with oxide growth, Journal of Nuclear Science and Technology. 52 (2015) 1259–1264. https://doi.org/10.1080/00223131.2015.1058196.

[52] B.D.C. Bell, S.T. Murphy, R.W. Grimes, M.R. Wenman, The effect of Nb on the corrosion and hydrogen pick-up of Zr alloys, Acta Materialia. 132 (2017) 425–431. https://doi.org/10.1016/j.actamat.2017.04.063.

[53] A. Couet, A.T. Motta, B. de Gabory, Z. Cai, Microbeam X-ray Absorption Near-Edge Spectroscopy study of the oxidation of Fe and Nb in zirconium alloy oxide layers, Journal of Nuclear Materials. 452 (2014) 614–627. https://doi.org/10.1016/j.jnucmat.2014.05.047.

[54] A. Garner, J. Hu, A. Harte, P. Frankel, C. Grovenor, S. Lozano-Perez, M. Preuss, The effect of Sn concentration on oxide texture and microstructure formation in zirconium alloys, Acta Materialia. 99 (2015) 259–272. https://doi.org/10.1016/j.actamat.2015.08.005.

[55] A. Motta, M. Gomes da Silva, A. Yilmazbayhan, R. Comstock, Z. Cai, B. Lai, Microstructural Characterization of Oxides Formed on Model Zr Alloys Using Synchrotron Radiation, Journal of ASTM International. 5 (2008) 1–20. https://doi.org/10.1520/JAI101257.

[56] J. Lin, H. Li, J.A. Szpunar, R. Bordoni, A.M. Olmedo, M. Villegas, A.J.G. Maroto, Analysis of zirconium oxide formed during oxidation at 623 K on Zr-2.5Nb and Zircaloy-4,

Materials Science and Engineering A. 381 (2004) 104–112. https://doi.org/10.1016/j.msea.2004.04.019.

[57] J. Liao, Z. Yang, S. Qiu, Q. Peng, Z. Li, J. Zhang, The correlation between tetragonal phase and the undulated metal/oxide interface in the oxide films of zirconium alloys, Journal of Nuclear Materials. 524 (2019) 101–110. https://doi.org/10.1016/j.jnucmat.2019.06.039.

[58] A. Garner, P. Frankel, J. Partezana, M. Preuss, The effect of substrate texture and oxidation temperature on oxide texture development in zirconium alloys, Journal of Nuclear Materials. 484 (2017) 347–356. https://doi.org/10.1016/j.jnucmat.2016.10.037.

[59] H. Li, M.G. Glavicic, J.A. Szpunar, A model of texture formation in ZrO2 films, Materials Science and Engineering A. 366 (2004) 164–174. https://doi.org/10.1016/S0921-5093(02)00787-6.

[60] N. Ni, D. Hudson, J. Wei, P. Wang, S. Lozano-Perez, G.D.W. Smith, J.M. Sykes, S.S. Yardley, K.L. Moore, S. Lyon, R. Cottis, M. Preuss, C.R.M. Grovenor, How the crystallography and nanoscale chemistry of the metal/oxide interface develops during the aqueous oxidation of zirconium cladding alloys, Acta Materialia. 60 (2012) 7132–7149. https://doi.org/10.1016/j.actamat.2012.09.021.

[61] B. Puchala, A. van der Ven, Thermodynamics of the Zr-O system from first-principles calculations, Physical Review B. 88 (2013) 094108. https://doi.org/10.1103/PhysRevB.88.094108.

[62] M. Parise, O. Sicardy, G. Cailletaud, Modelling of the mechanical behavior of the metal-oxide system during Zr alloy oxidation, Journal of Nuclear Materials. 256 (1998) 35–46. https://doi.org/10.1016/S0022-3115(98)00045-2.

[63] Y.S. Kim, M. Limback, B. Kammenzind, S.W. Dean, Role of Twinning and Slip in Deformation of a Zr-2.5Nb Tube, Journal of ASTM International. 5 (2008) 101120. https://doi.org/10.1520/JAI101120.

[64] K. Elbachiri, P. Doumalin, J. Crépin, M. Bornert, P. Barberis, V. Rebeyrolle, T. Bretheau, Characterization of local strain distribution in zircaloy-4 and M5® alloys, Journal of ASTM International. 5 (2008) 1–11. https://doi.org/10.1520/stp48136s.

[65] N. Ramasubramanian, P. v Balakrishnan, Aqueous Chemistry of Lithium Hydroxide and Boric Acid and Corrosion of Zircaloy-4 and Zr-2.5Nb Alloys, in: A.M. Garde, E.R. Bradley (Eds.), Zirconium in the Nuclear Industry: Tenth International Symposium, ASTM International, West Conshohocken, PA, 1994: pp. 378–399. https://doi.org/10.1520/STP15199S.

[66] N. Ramasubramanian, N. Precoanin, V. Ling, Lithium Uptake and the Accelerated Corrosion of Zirconium Alloys, in: Zirconium in the Nuclear Industry: Eighth International Symposium, ASTM International, 2008: pp. 187-201. https://doi.org/10.1520/stp18865s.

[67] S. Müller, L. Lanzani, Corrosion of zirconium alloys in concentrated lithium hydroxide solutions, in: Journal of Nuclear Materials, North-Holland, 2013: pp. 251–257. https://doi.org/10.1016/j.jnucmat.2012.07.030.

[68] V. Urbanic, B. Warr, A. Manolescu, C. Chow, M. Shanahan, Oxidation and Deuterium Uptake of Zr-2.5Nb Pressure Tubes in CANDU-PHW Reactors, in: Zirconium in the Nuclear Industry: Eighth International Symposium, ASTM International, 1989: pp. 20-34. https://doi.org/10.1520/stp18855s.

[69] S. Xie, B. Zhou, X. Liang, Q. Li, W. Liu, M. Yao, J. Zhang, The Distribution of Li Ions in the Oxide Film Formed on Zircaloy-4 Corroded in Lithiated Water at 633 K, Materials. 13 (2020) 873. https://doi.org/10.3390/ma13040873.